

# Pushing the limits: detecting H<sub>2</sub> emission from faint bipolar planetary nebulae in the IPHAS sample<sup>\*</sup>

G. Ramos-Larios<sup>1†</sup>, M.A. Guerrero<sup>2‡</sup>, L. Sabin<sup>3</sup> and E. Santamaría<sup>1,4</sup>

<sup>1</sup>*Instituto de Astronomía y Meteorología, Dpto. de Física, CUCEI, Universidad de Guadalajara, Av. Vallarta 2602, C.P. 44130, Guadalajara, Jalisco, Mexico*

<sup>2</sup>*Instituto de Astrofísica de Andalucía, IAA-CSIC, Glorieta de la Astronomía s/n, 18008 Granada, Spain*

<sup>3</sup>*Instituto de Astronomía, Universidad Nacional Autónoma de México, Apdo. Postal 877, C.P. 22860, Ensenada, B.C., Mexico*

<sup>4</sup>*Centro Universitario de Ciencias Exactas e Ingenierías, CUCEI, Universidad de Guadalajara, Av. Revolución 1500, Guadalajara, Jalisco, Mexico*

Last updated 2017 May 25; in original form 2017 Jan. 21

## ABSTRACT

We have obtained deep narrowband images in the near-IR H<sub>2</sub>  $\lambda$ 2.122  $\mu$ m emission line for a sample of 15 faint IPHAS bipolar planetary nebulae (PNe) to search for molecular material. H<sub>2</sub> emission is found in most of them (14 out of 15), mostly associated with rings at their equatorial regions and with their bipolar lobes. These detections add to the high occurrence of H<sub>2</sub> emission among bipolar PNe reported in previous works, resulting from the large reservoir of molecular material in these sources and the suitable excitation conditions for H<sub>2</sub> emission. The correlation between detailed bipolar morphology and H<sub>2</sub> luminosity is also confirmed: bipolar PNe with broad equatorial rings (R-BPNe) have almost no continuum emission, are H<sub>2</sub> brighter and have larger H<sub>2</sub>/Br $\gamma$  line ratio than bipolar PNe with pinched equatorial waists (W-BPNe). The origin of this dichotomy is unclear. The larger size and age of R-BPNe is consistent with shock excitation of H<sub>2</sub>, whereas UV pumping is most likely the excitation mechanism in the smaller and younger W-BPNe, which would explain their lower H<sub>2</sub> luminosity. Although both types of bipolar PNe seem to proceed from the same progenitor population, this does not imply that R-BPNe descend from W-BPNe. Otherwise, we note that some of the H<sub>2</sub>-weak bipolar PNe harbor post-common envelope binary systems and symbiotic stars. Finally, we suggest that the long-living H<sub>2</sub> emission from R-BPNe arises from a discrete distribution of compact knots embedded within the ionized gas at the equatorial region.

**Key words:** infrared: ISM – ISM: lines and bands – ISM: molecules – planetary nebulae: general

## 1 INTRODUCTION

Planetary nebulae (PNe) are the descendants of low- and intermediate-mass stars ( $\sim 0.8$ - $8 M_{\odot}$ ) caught in the short transition between the asymptotic giant branch (AGB) and white dwarf (WD) phases. PNe are routinely observed in optical emission lines that reveal the distribution and physical properties of ionized material, but these observations are insensitive to the dusty and molecular material remnant from the AGB phase. Infrared (IR) and radio observations can be used to detect this component in order to determine the full extent and outer geometry of PNe, to con-

strain the physical conditions in the regions dominated by dust and molecules (e.g., clumps and photo-dissociation regions, PDR), and ultimately to investigate the final episodes of mass-loss during the late AGB phase (see for example the works by Huggins et al. 1996; Young et al. 1999; Matsuura et al. 2005; Peretto et al. 2007; Phillips & Marquez-Lugo 2011).

Among the molecular tracers, the  $\nu = 1 \rightarrow 0$  S(1) 2.122  $\mu$ m molecular hydrogen (H<sub>2</sub>) emission line (hereafter we will refer to this line as H<sub>2</sub> unless otherwise stated) is one of the most common in PNe alongside carbon monoxide (CO) emission. Since the early IR observations of PNe, it has been noted that the H<sub>2</sub> emission has a higher occurrence rate among bipolar PNe (see, e.g., Zuckerman & Gatley 1988). Bipolar PNe have been suggested to descend from the most massive low- and intermediate-mass stars (Peimbert & Torres-Peimbert 1983; Corradi & Schwarz 1995).

Although there is a clear association of bipolar PN, type I PN and PN with a lower scale height, all pointing to a higher mass progenitor for bipolar PNe, it is not clear why the incidence of bipo-

<sup>\*</sup> Based on observations made with the William Herschel Telescope operated on the island of La Palma by the Isaac Newton Group in the Spanish Observatorio del Roque de los Muchachos of the Instituto de Astrofísica de Canarias.

<sup>†</sup> Contact e-mail: [gerardo@astro.iam.udg.mx](mailto:gerardo@astro.iam.udg.mx)

<sup>‡</sup> On sabbatical leave at the Instituto de Astronomía y Meteorología, Universidad de Guadalajara, Jalisco, Mexico

**Table 1.** Sample of IPHAS PNe observed with WHT LIRIS in the near-IR.

PNG	IPHASX J
G035.4+03.4	184336.6+034640 <sup>1</sup>
G038.9−01.3	190718.1+044056
G045.7+01.4	190954.7+120455 <sup>2</sup>
G045.7−03.8	192847.2+093436
G054.2−03.4	194359.5+170900
G057.9−00.7	194226.0+214521 <sup>3</sup>
G062.7+00.0	194940.9+261521
G062.7−00.7	195248.8+255359
G064.1−00.9	195657.6+265713
G068.0+00.0	200224.3+304845
G081.0−03.9	205527.2+390359 <sup>4</sup>
G091.6−01.0	212335.3+484717
G095.8+02.6	212608.3+542015
G101.5−00.6	221118.0+552841
G126.6+01.3	012507.9+635653

Other names:<sup>1</sup> PM 1-253, <sup>2</sup>Te 6, <sup>3</sup>Kn 7, <sup>4</sup>TEUTSCH PN J2055.4+3903.

lar PN,  $\sim 20\%$  (Parker et al. 2006), is larger than the fraction of stars that can produce a type I PN ( $\simeq 3.5 M_{\odot}$  main sequence stars, Karakas et al. 2009).

As such, they exhibit larger and thicker envelopes, with dense equatorial regions and compact clumps or knots that act as a shield against the UV radiation from their central stars (CSPNe), preventing the molecules’ dissociation. The association between H<sub>2</sub> emission and the bipolar morphological class has been thoroughly discussed by Kastner et al. (1996, 1994) who defined the so-called “*Gatley’s rule*”, automatically assimilating the presence of the H<sub>2</sub> 2.122  $\mu\text{m}$  emission line to a bipolar morphology. Although this is generally the case (Guerrero et al. 2000), sensitive observations reveal H<sub>2</sub> emission in PNe of morphological types other than bipolar (Marquez-Lugo et al. 2013; Akras, Gonçalves, & Ramos-Larios 2017).

It was also soon realized that the brightest H<sub>2</sub> emission was found at the equatorial regions of bipolar PNe with broad equatorial rings and a butterfly shape (Webster et al. 1988). These regions can be resolved into individual knots and dense clumps that are embedded within ionized material (Cox et al. 1998; Speck et al. 2002; Matsuura et al. 2009; Machado et al. 2015; Marquez-Lugo et al. 2015). On the other hand, PNe with a pinched-waist and a bow-tie shape have less prevalent H<sub>2</sub> emission which is furthermore associated to a PDR at their bipolar lobes (e.g., Hb 12, Dinerstein et al. 1988; Hora & Latter 1996). Following Marquez-Lugo et al. (2015), we will refer to the group of broad-ring bipolar PNe (i.e., “*butterflies*”) as R-BPNe, and to the group of pinched-waist bipolar PNe (i.e., “*bow-ties* or *hour-glasses*”) as W-BPNe.

Guerrero et al. (2000) investigated the H<sub>2</sub> over Br $\gamma$  line ratio in these two morphological sub-classes and concluded that R-BPNe have higher H<sub>2</sub> to Br $\gamma$  line ratios than W-BPNe. This is consistent with the H<sub>2</sub>-dominated and H I-dominated PNe described by Hora, Latter, & Deutsch (1999). The origin of this branching among bipolar PNe is unclear, but it may be related to the dominant excitation mechanism of the H<sub>2</sub> molecules in PNe. The H<sub>2</sub> emission line spectrum can be excited (*i*) by fluorescence or radiative pumping through the absorption of the UV radiation from the CSPN in a PDR (Black & van Dishoeck 1987; Dinerstein et al. 1988; Sternberg & Dalgarno 1989), or (*ii*) by shocked gas (Burton et al. 1992).

These excitation mechanisms result in notably different inten-

sities of the H<sub>2</sub> 1-0 S(1) line, being much brighter for shock-excited H<sub>2</sub>. Thus, Marquez-Lugo et al. (2015) used the very different efficiency of these two excitation mechanisms to argue that large H<sub>2</sub> 1-0 S(1) to Br $\gamma$  emission line ratios are indicative of shock excitation. They conclude that the H<sub>2</sub> brighter R-BPNe are preferentially excited by shocks, whereas the H<sub>2</sub> weaker W-BPNe are excited by UV fluorescence.

In this paper, we aim to extend the search for H<sub>2</sub> emission to PNe that are fainter than those included in previous works. If more evolved, these faint bipolar PNe can be used to investigate the evolution of the molecular content in bipolar PNe. The UWISH2 survey has detected H<sub>2</sub> emission from a number of bipolar PNe candidates which seems to be highly obscured, as they are not detected in H $\alpha$  (Froebrich et al. 2015; Gledhill et al. 2017). Similarly, the INT Photometric H $\alpha$  Survey data (IPHAS<sup>1</sup>; Drew et al. 2005; González-Solares et al. 2008; Barentsen et al. 2014) has unveiled a number of new faint PNe (e.g., Viironen et al. 2009). In particular, the IPHAS catalogue of extended PNe (Sabin et al. 2014) has revealed a set of 159 new true and possible PNe located in the Galactic Plane in the latitude range  $b = |5^{\circ}|$  among which 45 has been described as bipolar. This sample can be used to investigate the occurrence of H<sub>2</sub> emission among faint bipolar PNe. This research has also benefited from a new work on the estimation of distances to PNe (Frew, Parker, & Bojičić 2016). Otherwise, by selecting carefully sources whose nebular emission is not overimposed on crowded stellar fields, their H<sub>2</sub> fluxes can be measured accurately, contrary to nearby PNe with large angular sizes projecting onto multiple field stars.

The paper is organized as follows. Section §2 presents the sample and describes the selection criteria. The details of the new IR and archival optical observations that have been used in this work are given in section §3. The data reduction is also explained in this section. A discussion on the individual H<sub>2</sub> morphologies of each PNe and on their ionized and molecular distributions is presented in §4, as well as the different morphological groups which can be drawn from our sample. Finally a general discussion, including here the sample from Guerrero et al. (2000), and the conclusions are presented in §5 and §6, respectively.

## 2 SAMPLE

We selected a set of fifteen PNe from the IPHAS sample of true and possible PNe (Sabin et al. 2014) mostly based on H $\alpha$ + [N II] morphologies indicative of the presence of bipolar lobes collimated by equatorial rings or waists. To maximize their detection, we chose PNe which were optically “bright” among IPHAS sources, implying H $\alpha$  dereddened peak fluxes up to  $10^{-14}$  erg cm<sup>-2</sup> s<sup>-1</sup>.

Furthermore, to assess the H<sub>2</sub> spatial distribution, we selected sources large enough to be resolved, but not too large so they can fit within the field of view (FoV) of the instrument used for these observations (see below). An additional selection criterium requires minimizing the number of field stars overimposed on the optical nebular emission. Thus our sample includes PNe with optical diameters (major axis) ranging from  $\sim 9''$  to  $\sim 78''$ .

The IAU-PNG and IAU-IPHAS designations of the PNe in our sample (the latter includes their J2000 equatorial coordinates) are listed in columns 1 and 2 of Table 1. Detailed information of these sources can be found in the HASH database

<sup>1</sup> <http://www.iphas.org/>

**Table 2.** Filters characteristics for each instrument used in the present study.

Telescope/Instrument	Filter	$\lambda_c$	$\Delta\lambda$
WHT/LIRIS	H <sub>2</sub>	2.122 $\mu\text{m}$	0.032 $\mu\text{m}$
	Kc	2.270 $\mu\text{m}$	0.034 $\mu\text{m}$
INT/WFC	H $\alpha$	6568 $\text{\AA}$	95 $\text{\AA}$

(Parker, Bojčić, & Frew 2016). We note that according to the HASH database, G035.4+03.4 classification has become symbiotic star (SS), and G038.9–01.3 and G062.7–00.7 are now flagged as likely PN. For the especial case of G054.2–03.4, a post-common envelope (CE) binary, must be treated carefully about our findings.

### 3 OBSERVATIONS

#### 3.1 Near-IR imaging

Narrow-band H<sub>2</sub> 2.122  $\mu\text{m}$  and  $K_c$  continuum near-IR images were obtained with the Long-slit Intermediate Resolution Infrared Spectrograph (LIRIS: Machado et al. 2003; Acosta Pulido et al. 2003) at the 4.2m William Herschel Telescope (WHT) on Roque de Los Muchachos Observatory (ORM: La Palma, Spain). The characteristics of the filters are shown in Table 2. The detector is a 1024 $\times$ 1024 HAWAII array with plate scale of 0''.25 pixel<sup>-1</sup> and an FoV of 4'.27 $\times$ 4'.27.

Most observations were carried out on 2014 July 13. One object, IPHASXJ194359.5+170900 (a.k.a., the Necklace nebula, Sabin 2008; Corradi et al. 2011; Miszalski et al. 2013) has been previously observed on the same telescope on 2007 September 19. We acquired 16 $\times$ 60s exposures in H<sub>2</sub> and 8 $\times$ 60s exposures in  $K_c$  for each object during the most recent run, and 150 $\times$ 20s exposures during the 2007 run. The IR observing procedure which includes images jittering has been described in details by Ramos-Larios et al. (2012)<sup>2</sup>. The data reduction was performed using the package LIRISDR (LIRIS Data Reduction), which is an IRAF<sup>3</sup>-based pipeline dedicated to the automatic reduction of near-IR data. The processing steps include bad pixel mapping, cross-talk correction, flat-fielding, sky subtraction, removal of reset anomaly effect, field distortion correction, and co-addition to form the final image. The procedure is repeated for each H<sub>2</sub> and  $K_c$  data-sets separately. The latter, which corresponds to the continuum emission, is subsequently scaled and subtracted from its H<sub>2</sub> image counterpart. The new near-IR images are presented in Figures 1, 2, 3 and 4 arranged by their Galactic longitude.

It is worth emphasizing the high throughput and efficiency of the LIRIS instrument at the WHT in terms of detection of molecular hydrogen at low surface brightness levels. M2-48 and NGC 6778 were reported as H<sub>2</sub>-free by Kastner et al. (1996) and Webster et al. (1988), respectively, but recent WHT LIRIS observations actually detected H<sub>2</sub> emission (Marquez-Lugo et al. 2013). This is critical for this project, as we initially deal with even fainter optical PNe than M2-48 and NGC 6778.

<sup>2</sup> See also the WHT/LIRIS website at:

<http://www.ing.iac.es/Astronomy/instruments/liris/imaging.html>

<sup>3</sup> IRAF (Image Reduction and Analysis Facility) is distributed by the National Optical Astronomy Observatories, which are operated by the Association of Universities for Research in Astronomy, Inc., under cooperative agreement with the National Science Foundation.

#### 3.2 Optical imaging

The optical images presented in this article were retrieved from the IPHAS images data bank<sup>4</sup>. These images were originally obtained with the Wide Field Camera (WFC) mounted on the 2.5m Isaac Newton Telescope (INT), also located at the ORM. The camera has a FoV of 34 $\times$ 34 arcmin<sup>2</sup> and a plate scale of 0''.33 pixel<sup>-1</sup>. The properties of the H $\alpha$  filter used during the survey are given in Table 2. We note that the H $\alpha$  filter also contains the [N II]  $\lambda$ 6583  $\text{\AA}$  emission line (Drew et al. 2005). We will therefore refer to these as H $\alpha$ +[N II] images. Exposure times were always 120 s.

These images were combined with the near-IR images to create the colour-composite pictures presented in the *right* panels of Figures 1, 2, 3 and 4.

### 4 BASIC MORPHOLOGY IN THE NEAR-IR H<sub>2</sub> LINE

All the sources in our sample, but PNG045.7+01.4 (a.k.a. Te 6), are detected in H<sub>2</sub>. Te 6 is a barrel-like PN with broad *ansae* which can be interpreted as bipolar lobes. The nebula has a diameter of 17''.3 $\times$ 13''.8 in the H $\alpha$  line (Fig. 1). The optical emission is mostly localized in a broad, diffuse equatorial region, whereas the polar protrusions (particularly the Southern one) are much fainter.

According to the morphology and intensity of the H<sub>2</sub> emission, the sources in our sample with detected H<sub>2</sub> emission can be organized into two different groups. PNe with equatorial pinched waist (i.e., W-BPNe) have typically faint H<sub>2</sub> emission (e.g., PNG035.4+03.4, Fig. 1), whereas those with a well developed equatorial ring (i.e., R-BPNe) tend to have bright H<sub>2</sub> emission (e.g., PNG126.6+01.3, Fig. 4). These two groups are described into more detail below.

#### 4.1 W-BPNe: PNe with pinched equatorial waists

This group includes PNG035.4+03.4, G038.9–01.3 (Figure 1), and G062.7–00.7 (Figure 3). The optical morphology of these PNe is characterized by narrow waists in between a pair of bipolar lobes (PNG035.4+03.4), a highly collimated bipolar outflow (PNG038.9–01.3), and a pair of hourglass-shaped bipolar lobes (PNG062.7–00.7).

In the near-IR continuum  $K_c$  filter, they show mostly compact, bright emission in the innermost regions, whereas the images in the H<sub>2</sub> filter show additional extended emission along the collimated structures. (Fig. 1, and 3 *left and middle-left*). The continuum subtracted images (Fig. 1, and 3 *middle-right*) reveal the lack of 2.122  $\mu\text{m}$  H<sub>2</sub> emission in the innermost regions, being the molecular emission mostly restricted to the collimated structures. Otherwise, the details of the diffuse H<sub>2</sub> emission differs among these three sources.

##### • PNG035.4+03.4 (a.k.a. PM 1-253)

The 2.122 $\mu\text{m}$  H<sub>2</sub> emission traces the onset of the bipolar ejections, much smaller in size than the  $\sim$ 9''.6 emission detected in the H $\alpha$ + [N II] IPHAS image (Fig. 1). The eastern side of the equatorial plane seems to present very faint H<sub>2</sub> emission, but we reckon it may be an artifact caused by a defective subtraction of the bright continuum emission. The distribution of the H<sub>2</sub> region is somehow similar to that described for M2-9 (Phillips et al. 1985; Kastner et al. 1996), although the detailed morphology is not that

<sup>4</sup> <http://www.iphas.org/images/>

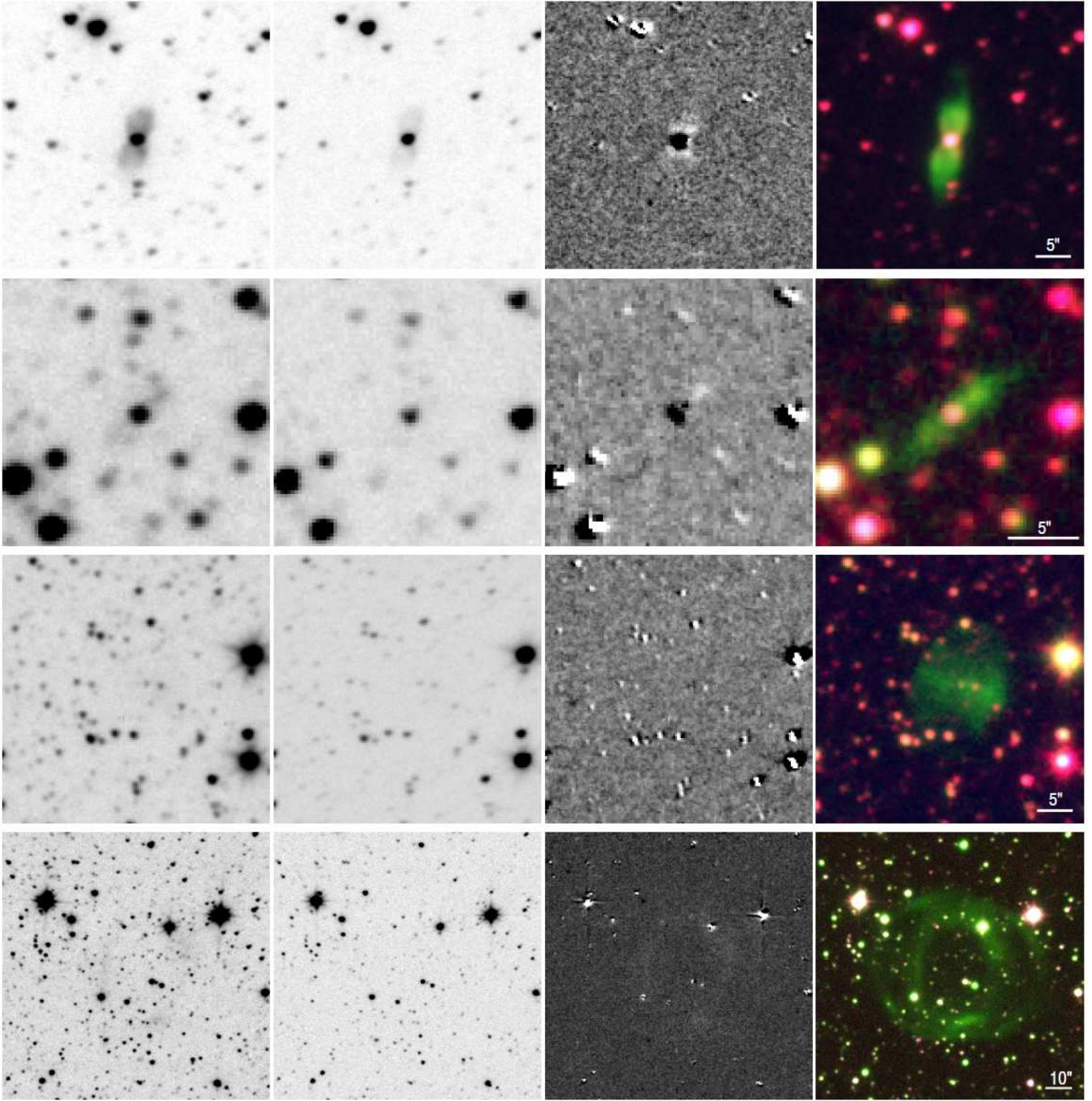


**Figure 1.** WHT LIRIS near IR images (*from top to bottom*) of PN G035.4+03.4, PN G038.9-01.3, PN G045.7+01.4 and PN G045.7-03.8 in the  $H_2$ ,  $K_c$ , continuum-subtracted  $H_2 - K_c$  filters and a colour-composite WHT  $H_2$  (red), IPHAS  $H\alpha + [NII]$  (green), and WHT  $K_c$  (blue) (*from left to right, respectively*). In all images, north is top, east to the left. The spatial scale is shown in the last colour panel.

close. The  $H_2$  emission in M2-9 follows the walls of the bipolar lobes in their full extent, what has been referred to as a “thin  $H_2$  skin” (Hora & Latter 1994; Smith et al. 2005), whereas in the “IPHAS counterpart” PN G035.4+03.4 it is concentrated at the base of the lobes.

- PN G038.9-01.3

The molecular hydrogen emission is mostly detected along the collimated outflow, with the north-west component of the outflow being brighter than the south-east one (Fig. 1). The asymmetry of the  $H_2$  emission could be interpreted as the result of asymmetric

mass loss, but also produced by an orientation effect causing higher extinction to the south-east region. In this sense, the  $H\alpha + [N II]$  IPHAS image also reveals brighter emission of the north-west region. The nebular morphology of PN G038.9-01.3 is rather similar to that of M1-91 (Guerrero et al. 2000). The latter has been classified as an SS (e.g. Schmeja & Kimeswenger 2001), whereas PN G038.9-01.3 is flagged as a likely PN in the HASH database (Parker, Bojičić, & Frew 2016).

- PN G062.7-00.7

The  $H_2$  emission follows the ionized emission seen in the light of

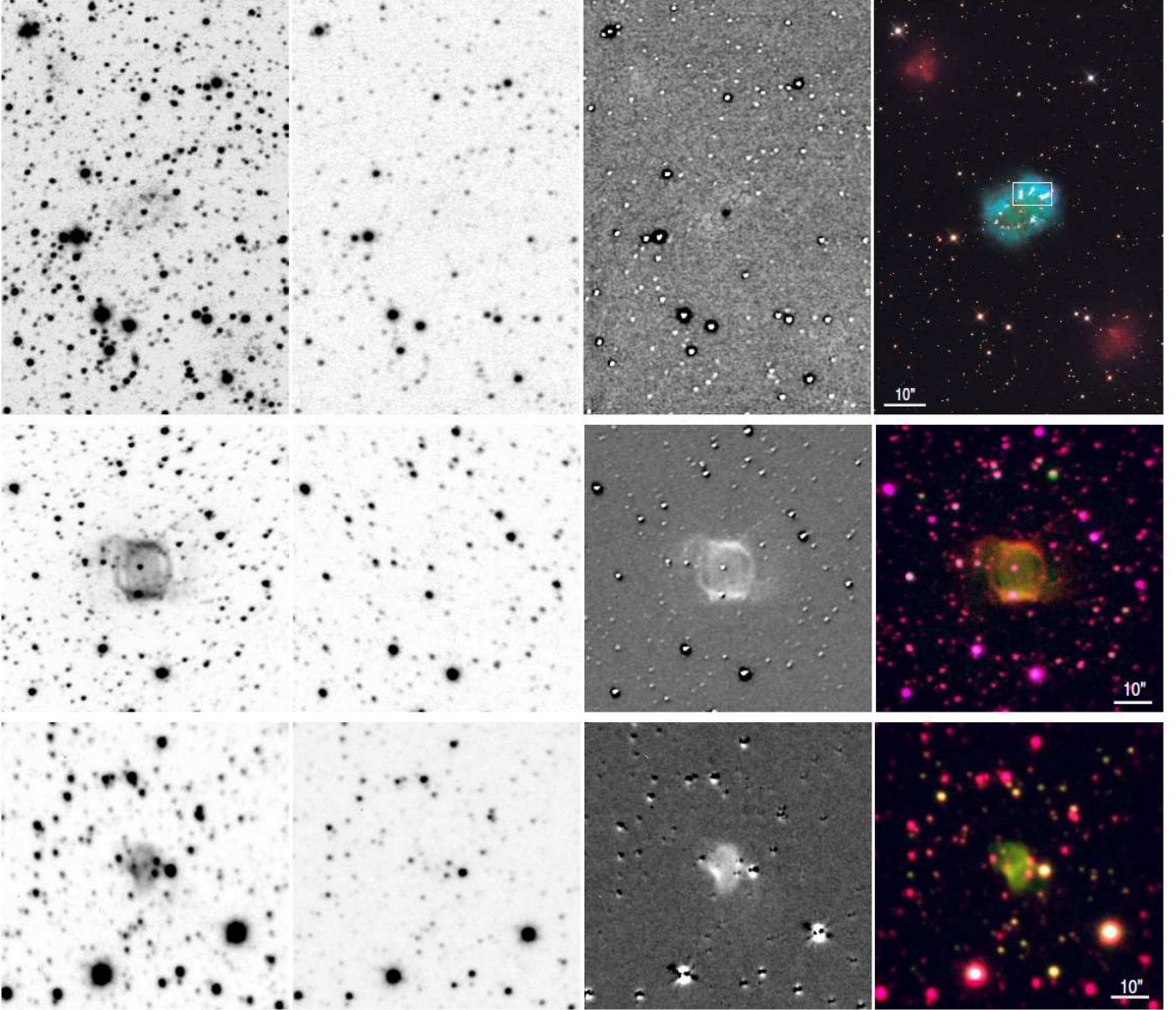


**Figure 2.** Same as Fig. 1 (from top to bottom) for PN G054.2–03.4, PN G057.9–00.7 and PN G062.7+00.0. In this case, the right panel of PN G054.2–03.4 show a colour-composite *HST* WFC3 [N II] (red), H $\alpha$  (green), and [O III] (blue) picture. The small box in the same panel corresponds to the image section shown in Figure 5. *HST* image courtesy of the Hubble Heritage Team (STScI/AURA).

H $\alpha$ + [N II] (Fig. 3). The H $_2$  data indicate a total size of  $\sim 61''5$ . The H $_2$  emission from the central region is located in the outermost region, enclosing the pinched waist.

In many ways, the spatial distribution of the H $_2$  emission from this IPHAS PN that encloses the optical emission from the bipolar outflows is similar to that shown in the WHT continuum-subtracted H $_2$  2.122  $\mu\text{m}$  image of the well-known bipolar PN NGC 6537 (Marquez-Lugo et al. 2013). The HASH database casts doubts on the PN nature of this source and flags it as a likely PN (Parker, Bojčić, & Frew 2016).

#### 4.2 R-BPNe: PNe with broad equatorial rings

This group includes the remaining PNe in our sample, namely PN G045.7–03.8, G045.7–03.8, G057.9–00.7, G062.7+00.0, G064.1–00.9, G068.0+00.0, G081.0–03.9, G091.6–01.0,

G095.8+02.6, G101.5–00.6, and G126.6+01.3. These PNe are characterized by the presence of large equatorial rings or broad structures that are at the origin of bipolar lobes or other axisymmetrical structures such as ansae or protrusions.

In the near-IR, these sources show basically no emission in the  $K_c$  continuum images. The diffuse H $_2$  emission is spatially coincident with the optically brighter equatorial structure and, in a few cases, with the fainter bipolar components. The intensity of the H $_2$  emission echoes that seen in the H $\alpha$ + [N II] IPHAS images, with brighter emission in the equatorial regions. We describe briefly the H $_2$  morphology of some individual sources.

- PN 045.7–03.8

The optical images show two interleaved circular rings  $\sim 58''1 \times 68''2$  in size with brighter emission in the central regions where they overlap. Weak H $_2$  emission is detected in the

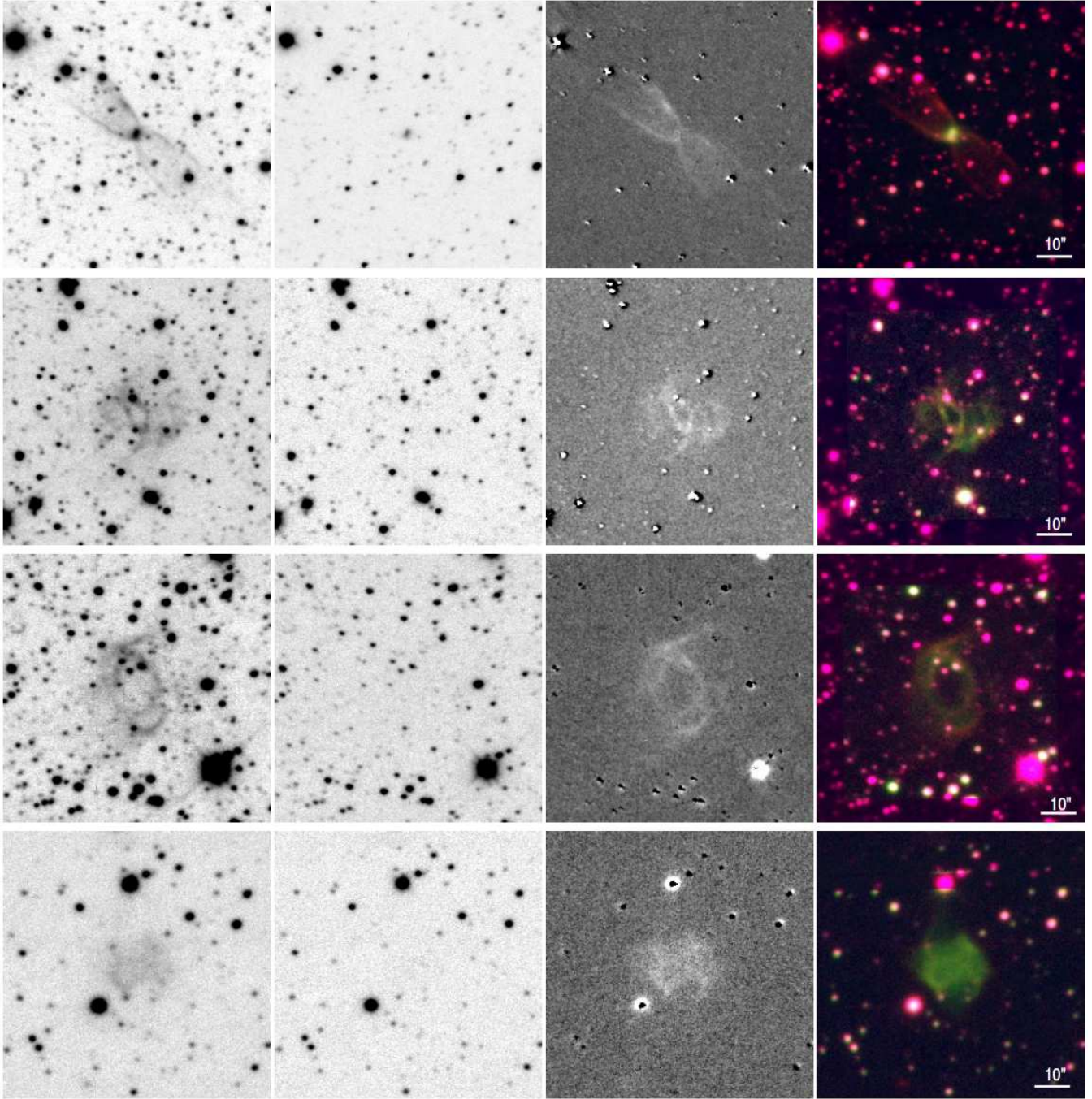


**Figure 3.** Same as Fig. 1 (from top to bottom) for PN G062.7–00.7, PN G064.1–00.9, PN G068.0+00.0 and PN G081.0–03.9.

central regions, spatially coincident with the brightest patches in the  $H\alpha+[N\ II]$  IPHAS image (Fig. 1).

- PN G054.2–03.4 (a.k.a. the Necklace Nebula)

The optical images of the Necklace Nebula show a knotty ring and a pair of high velocity collimated outflow/jets. These have been presumably launched from an accretion disk before the common envelope phase of the close binary system formed by its central star and a carbon dwarf companion (Corradi et al. 2011; Miszalski et al. 2013). The  $2.122\ \mu\text{m}$   $H_2$  emission arises exactly at the location of the ionized knots, but also at the polar caps (Figure 2). The  $H_2$  surface brightness in this PN is extremely low and its detection

required an integration time about three times longer than that for the other objects in our sample.

The detailed image of the Northwest quadrant of the equatorial ring of the Necklace Nebula shown in Figure 5 is revealing. The  $H_2$  emission comes from a discrete distribution of compact knots and filaments associated with the  $[N\ II]$  knots and their tails, rather than from a classical PDR. This is very similar to the distribution of the  $H_2$ -emitting knots embedded in the equatorial regions of NGC 650-51 (Marquez-Lugo et al. 2015) and NGC 2346 (Manchado et al. 2015), but also in the low-ionization features (FLIERS) of NGC 7662 (Akraş, Gonçalves, & Ramos-Larios 2017). It is worth emphasizing the varying spatial distribution of the molecular and

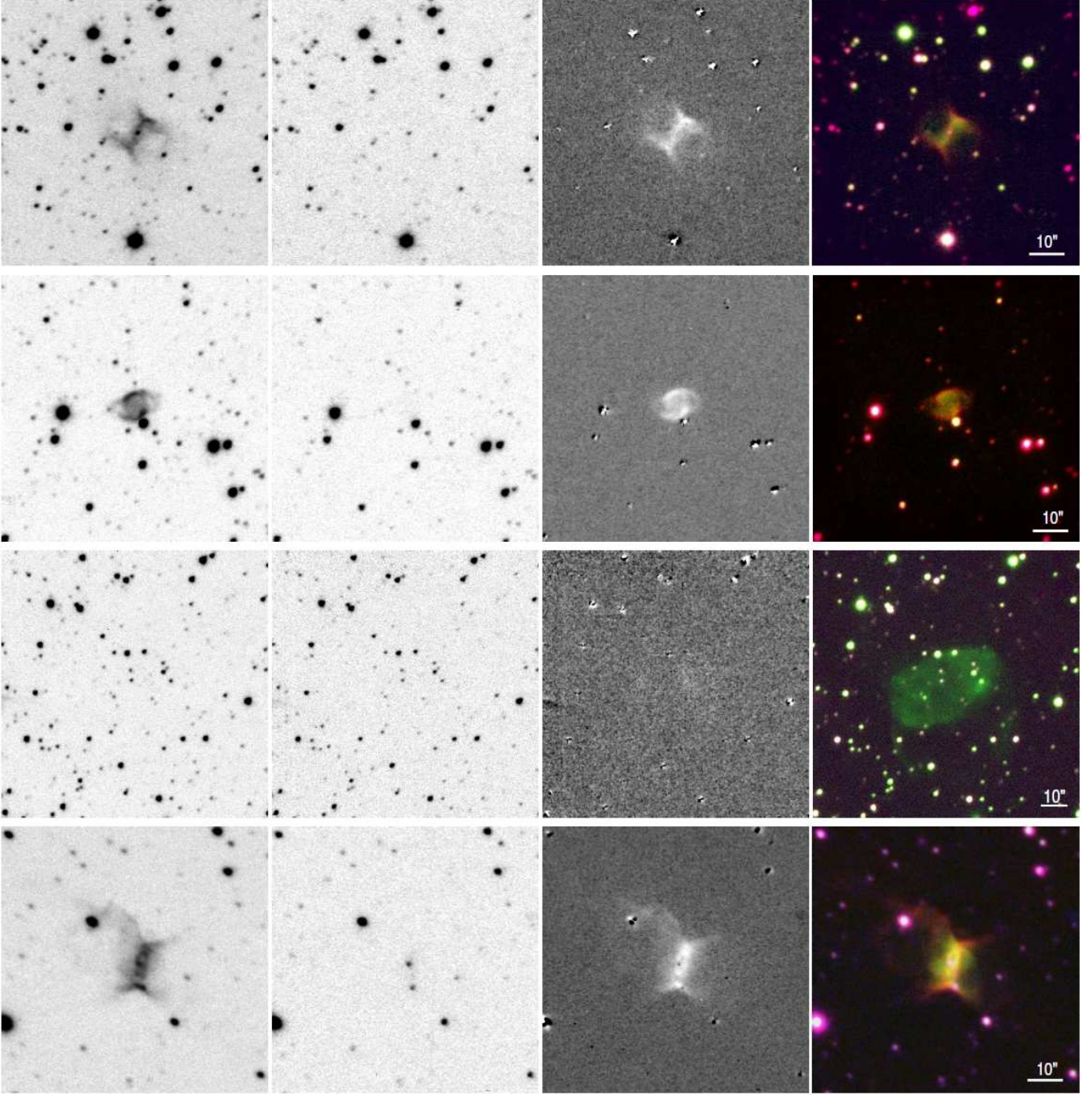


**Figure 4.** Same as Fig. 1 (from top to bottom) for PN G091.6–01.0, PN G095.8+02.6, PN G101.5–00.6 and PN G126.6+01.3.

low-ionization material in these knots; sometimes the  $\text{H}_2$  emission in the knot faces the central star and the  $[\text{N II}]$  emission lies beyond (for instance, the central knot in Fig. 5), but in some other cases the  $\text{H}_2$  emission seems to peak further away from the central star than the  $[\text{N II}]$  emission (as in the two other knots in Fig. 5). This may reveal projection effects, suggesting that the  $\text{H}_2$  and  $[\text{N II}]$  emissions are not coplanar. Certainly, an  $\text{H}_2$  image of spatial resolution similar to that of the *HST* WFC  $[\text{N II}]$  image is required to investigate the details of the varying spatial distribution of molecular and low-ionisation material in this nebula.

- PN G057.9–00.7 (a.k.a. Kn 7)

The optical images reveal a bipolar PN showing a bright central

ring partially filled with ionized material and faint bipolar lobes. The  $\text{H}_2$  emission follows the spatial location of the  $\text{H}\alpha + [\text{N II}]$  emission, being particularly bright in the ring and relatively fainter in its interior (Figure 2). The bipolar lobes are also detected in the  $\text{H}_2$  image.

- PN G062.7+00.0

The optical image shows a butterfly nebula with size  $\sim 18''.5 \times 11''.0$  and a bright wide waist. The  $\text{H}_2$  emission largely covers the whole ionized region, with stronger emission in the waist (Fig. 2).

- PN G064.1–00.9 and PN G068.0+00.0

Bipolar PNe with an equatorial ring and two diffuse bipolar outflows. There is an excellent spatial match between the  $\text{H}_2$  and op-

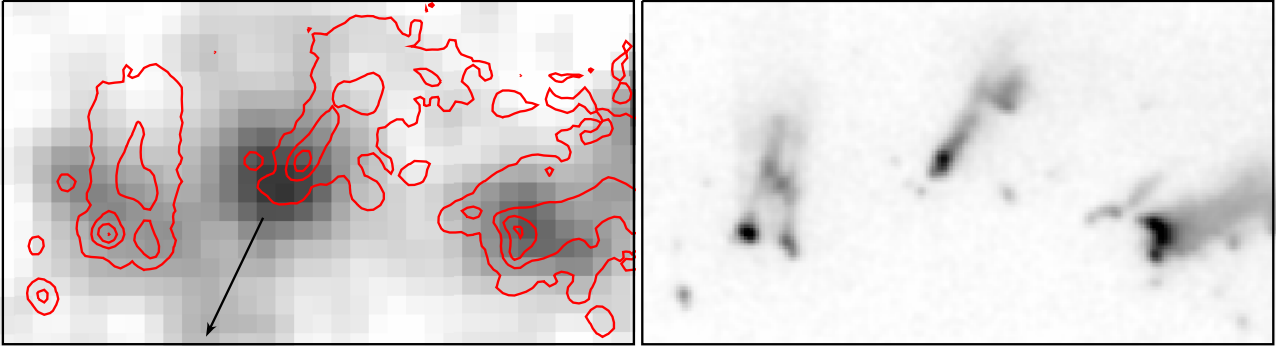


**Figure 5.** Zoom of the North-western knots in the ring of the Necklace Nebula in  $H_2$  (left) and  $[N\ II]$  (right).  $[N\ II]$  contours are overlotted on the  $H_2$  image. The arrow in the  $H_2$  image points to the central star. The FoV is  $8''.5 \times 5''.0$ .

tical  $H\alpha+[N\ II]$  morphologies, with the equatorial ring being the brightest structure (Fig.3).

- PN G081.0–03.9

Bipolar PN with an open barrel-like structure from whose tips protrude fainter bipolar extensions. The  $H_2$  emission is rather diffuse and located at the barrel-like feature, i.e., the brightest region of the optical  $H\alpha+[N\ II]$  emission (Fig.3).

- PN G091.6–01.0 and PNG126.6+01.3 (a.k.a. “Principe de Asturias” Nebula)

Bipolar PNe with a classical *butterfly* morphology viewed side-on (Figs. 4). The central rings are thus seen mostly as bars or very elongated ellipses. Both nebulae exhibit stars located very close to the centre of the nebular equatorial regions. Molecular hydrogen is detected along the central bars, enveloping the tips of the equatorial rings, as well as at the outer walls of the bipolar lobes.

- PN G095.8+02.6

Bipolar PN with a remarkable point-symmetric morphology. The spatial distribution of the molecular hydrogen confirms this point-symmetric morphology (Fig.4). Molecular emission is detected in the main nebular shell, and faintly at the *ansae*.

- PN 101.5–00.6

The optical image displays an equatorial structure and two fainter bipolar lobes. The emission in the  $H\alpha+[N\ II]$  IPHAS image is suggestive of a broad equatorial belt seen from the side, so that the bipolar lobes lie on the plane of the sky. The  $H_2$  emission is extremely poor and only a patchy feature is seen towards the brighter north-western edge of the optical emission (Fig.4).

## 5 DISCUSSION

### 5.1 General properties of the $H_2$ emission in the IPHAS sample of PNe

This study confirms the prevalence of  $H_2$  emission among bipolar PNe: only one source (PNG045.7+01.4) out of 15 bipolar PNe in this sample shows no trace of  $H_2$  emission in its continuum-subtracted  $H_2$  image (Fig. 1).

Narrow-band near-IR imaging of a combined sample of 141 PNe (Kastner et al. 1996; Guerrero et al. 2000; Marquez-Lugo et al. 2015; Akas, Gonçalves, & Ramos-Larios 2017, this work) support this prevalence:  $\sim 75\%$  (66 out of 89) of bipolar PNe are detected in  $H_2$ , whereas only  $\sim 25\%$  (13 out of 52) of non-bipolar PNe are detected in  $H_2$ .

The  $H_2$  emission originates from the equatorial regions and bipolar lobes of the PNe in the IPHAS sample. Whenever there is

a broad ring-like structure (i.e., in the 11 R-BPNe with  $H_2$  emission), the  $H_2$  emission is brighter in these regions than in the bipolar lobes. This is the case even for the faint source PNG101.5–00.6 whose bipolar lobes are most likely missing detection. In the remaining three sources that show a pinched-waist (the W-BPNe sources PNG035.4+03.4, G038.9–01.3, and G062.7–00.7), the  $H_2$  emission is brighter in the bipolar lobes, whereas the central regions are dominated by continuum emission. Continuum emission in R-BPNe is basically negligible, pointing to the absence of dust thermal emission.

When the spatial distributions of the emission from molecular and ionized material can be compared, it can be seen that the innermost regions close to the central star are dominated by ionized material. Molecular material, as traced by the  $H_2$  emission, is confined to the outer edges of the ionized regions (Beckwith, Gatley, & Persson 1978).

The preferential detection of  $H_2$  emission associated with the equatorial regions of bipolar PNe and its distribution at the outer edges of these confirm that equatorial density enhancements provide ideal conditions to shelter the  $H_2$  molecule from UV radiation and avoid its dissociation. However, the detailed comparison between the molecular  $H_2$  and low-ionization  $[N\ II]$  emissions for the North-west quadrant of the equatorial ring of the Necklace Nebula (Fig. 5) suggests that the  $H_2$  emission arises from knots and filaments which are spatially coincident with the  $[N\ II]$  knots. When deep  $H_2$  and optical observations of the highest spatial resolution are obtained, they unveil that the molecular material in the equatorial regions of bipolar PNe is embedded within ionized gas (e.g., Manchado et al. 2015).

### 5.2 Prevalence of $H_2$ or H I emission.

The prevalence of the emission from the  $H_2\ 1-0\ S(1)$  line over  $Br\gamma$  is commonly used to classify sources into molecular- or ionized-dominated (e.g., Hora, Latter, & Deutsch 1999). This classification is useful to investigate the evolutionary stage of the nebula (e.g., Aleman & Gruenwald 2011; Likkell et al. 2006) or possible different evolutionary paths (Guerrero et al. 2000).

As noted in Section §1, this same ratio has been associated with different bipolar morphologies: R-BPNe show brighter  $H_2$  than  $Br\gamma$ , whereas W-BPNe have brighter  $Br\gamma$  than  $H_2$  (Guerrero et al. 2000; Marquez-Lugo et al. 2015).

In this context, it is worthwhile to investigate the relative intensity of the  $H_2\ 1-0\ S(1)$  and  $Br\gamma$  emission lines in the IPHAS sample and compare them to those presented by Guerrero et al. (2000).

The  $H_2$  1-0 S(1) fluxes of the PNe in our sample can be derived from the WHT LIRIS images. First, we have used an aperture encompassing the whole nebular extent of each PN to derive the total count rate. This has been also estimated for a number of stars in the field of view using IRAF DIGIPHOT routines. The count rates from these stars are then compared to their 2MASS  $K_s$  magnitudes to derive a photometric zero point magnitude. Then, taken into account the filter transmission curve to derive the filter equivalent width (EW), the count rates of the nebular emission in the  $H_2$  1-0 S(1) line have been converted into observed fluxes. For bright sources, the flux uncertainty is dominated by the Poisson statistics and it may range from 5% to 20%. For faint and extended sources, the flux uncertainty can amount up to 50%.

Similarly, the IPHAS images can be used to determine the  $Br\gamma$  fluxes of these sources. The images are used to obtain the count rates in the INT  $H\alpha$ + $[N\ II]$  filter. Optical spectroscopic observations obtained for these sources in the IPHAS framework (Sabin et al. 2014) are used in conjunction with the filter transmission curve to assess and subtract the contribution of the  $[N\ II]\ \lambda\lambda 6548, 6584$  lines to the emission detected in the IPHAS  $H\alpha$ + $[N\ II]$  image. The net  $H\alpha$  count rate is then converted into observed flux<sup>5</sup> using the zero point magnitude  $z_p$  provided by Barentsen et al. (2014). This flux is corrected from extinction using the  $H\beta$  logarithmic extinction coefficient,  $c(H\beta)$ . This is derived from the observed  $H\alpha$  to  $H\beta$  flux ratio measured in the IPHAS optical spectra compared to the theoretical ratio expected for Case A at 10,000 K (Osterbrock & Ferland 2006). For those sources with no available optical spectra covering the  $H\alpha$  and  $H\beta$  emission lines (namely, PN G035.4+03.4, G045.7–03.8, G054.2–03.4, G062.7+00.0, and G062.7–00.7),  $c(H\beta)$  was computed from their H I column density provided by Dickey & Lockman (1990) and Kalberla et al. (2005) assuming the gas-to-dust ratio from Bohlin, Savage, & Drake (1978). The intrinsic  $Br\gamma$  flux is then derived using the theoretical  $Br\gamma$  to  $H\alpha$  flux ratio of 0.00990 which can be derived using Osterbrock & Ferland (2006) theoretical line ratios for case A at 10,000 K. To allow a fair comparison between the  $H_2$  1-0 S(1) and  $Br\gamma$  fluxes, the flux from the former line is also dereddened using the measured  $c(H\beta)$ .

The intrinsic  $H_2$  and  $Br\gamma$  fluxes and the  $[N\ II]\ \lambda 6584$  to  $H\alpha$  and  $H_2$  to  $Br\gamma$  ratios are collected in Table 3. The detailed bipolar morphological sub-types (R-BPNe and W-BPNe) are also included in this Table. For completeness, the sample of bipolar PNe in Guerrero et al. (2000) has been added to this table. The  $H_2$  flux of NGC 6881 listed by Guerrero et al. (2000) is considered to be a lower limit in view of the deeper  $H_2$  images presented by Ramos-Larios, Guerrero, & Miranda (2008).

The trends are shown in Figures 6, 7, and 8. The new IPHAS PNe extend towards regions of lower  $H_2$  and  $Br\gamma$  fluxes (Figure 6-left). In agreement with previous results, R-BPNe have generally larger  $H_2$  than  $Br\gamma$  fluxes, whereas W-BPNe are typically fainter in  $H_2$  than in  $Br\gamma$ . All R-BPNe are detected in  $H_2$  with the only exception of Hen 2-428 and PN G045.7+01.4. Most R-BPNe have  $H_2/Br\gamma$  ratios above unity, with the exceptions of PC 20, M 1-59, the Necklace Nebula, and PN G101.5–00.6. Most W-BPNe have  $H_2/Br\gamma$  ratios below unity, with the only exceptions of NGC 6881 and PN G062.7–00.7. These exceptions are labeled in Figure 6-left.

<sup>5</sup> No spectrum in the spectral range covering the  $H\alpha$  and  $[N\ II]$  emission lines is available for PN G035.4+03.4. The  $H\alpha$  flux for this nebula has not been corrected from the  $[N\ II]$  contribution, and thus it provides an upper limit of its true  $H\alpha$  flux.

There is also a notable correlation between the near-IR  $H_2/Br\gamma$  and optical  $[N\ II]/H\alpha$  line ratios (Figure 6-right); sources with larger  $H_2/Br\gamma$  line ratios tend to show also larger  $[N\ II]/H\alpha$  line ratios. Furthermore, R-BPNe do not only have the largest  $H_2/Br\gamma$  ratios, but they also show the largest  $[N\ II]/H\alpha$  line ratios. Most R-BPNe have  $H_2/Br\gamma$  line ratios  $\geq 10$ , thus implying shock excitation (Marquez-Lugo et al. 2015). Similarly, the low  $H_2/Br\gamma$  line ratio of most W-BPNe implies UV excitation.

### 5.3 The $H_2$ Luminosity Distribution and Physical Properties of BPNe

The  $H\alpha$  intrinsic flux of each source has been combined with its size according to the prescriptions of Frew, Parker, & Bojić (2016) to derive its distance. The distribution of the sources in the Galaxy is shown in Figure 7. Whereas the sources sampled by Guerrero et al. (2000) are generally closer than 5 kpc ( $4.2 \pm 1.2$  kpc in average), the IPHAS sources are mostly distributed above 5 kpc from the Sun ( $8.4 \pm 3.8$  kpc in average), with some of them as far as 15 kpc. This results confirms that the IPHAS sample of bipolar PNe presented in this work probes sources at further distances in the Galaxy. Meanwhile, the faintest  $H\alpha$  bipolar PNe sampled by UWISH2 (Froebrich et al. 2015) correspond to very extinguished sources or even to sources that have not been ionized yet (Gledhill et al. 2017).

The distance is then used to derive the luminosity in the  $H_2$  and  $Br\gamma$  emission lines of these BPNe, as well as their Galactic height and linear size. The comparison between the  $H_2$  and  $Br\gamma$  luminosities (Figure 8-left) confirms that both samples of bipolar PNe are rather similar, with the IPHAS sample being generally only a bit fainter than the bipolar PNe sampled by Guerrero et al. (2000). The low  $H\alpha$  surface brightness of the bipolar PNe in the IPHAS sample does not imply these are more evolved sources, but rather more distant and extinguished.

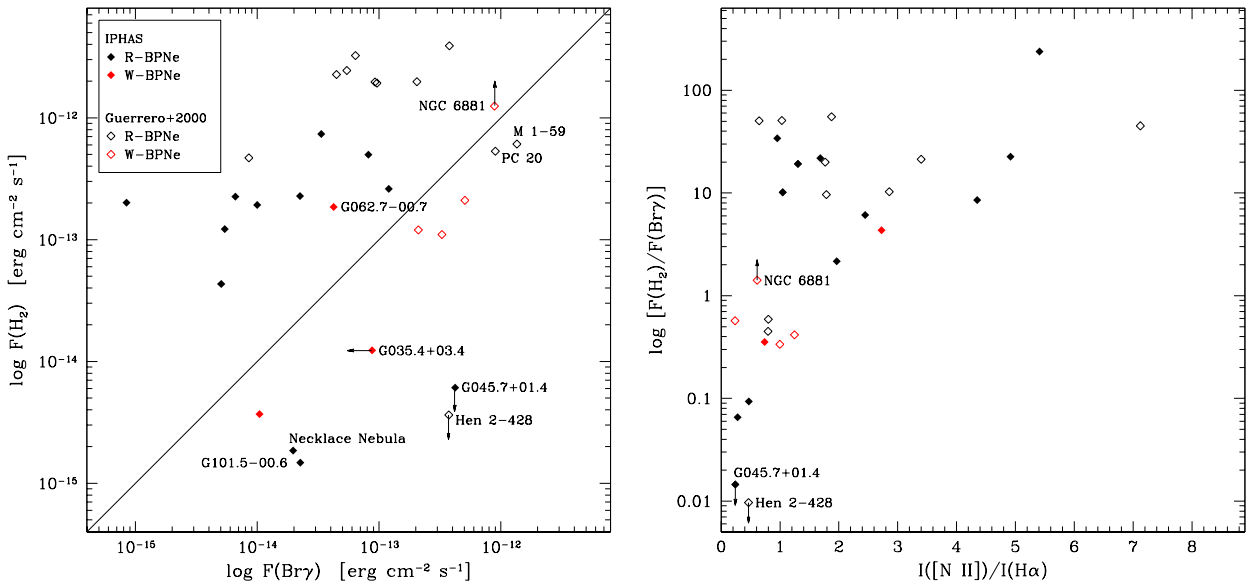
W-BPNe have typically larger  $Br\gamma$  luminosities than R-BPNe, whereas the opposite is true for  $H_2$ . There are two outstandingly faint  $H_2$  R-BPNe in this plot, namely the Necklace Nebula and PN G101.5–00.6. The former has been claimed to be a post-AGB/post-PN ejecta nebula (Miszalski et al. 2013).

As for the correlation between PN size and  $H_2$  luminosity (Figure 8-right), W-BPNe ( $0.28 \pm 0.10$  pc) are notably smaller than R-BPNe ( $0.56 \pm 0.29$  pc). The latter show a notable flat distribution of  $H_2$  luminosity with size, i.e., the nebular size does not affect the  $H_2$  luminosity. If nebular size can be correlated with nebular age (assuming similar expansion velocities), then the above result implies that there is very little evolution of the total  $H_2$  luminosity with age and expansion for R-BPNe. As  $H_2$  emission is still detectable (and bright) in very extended and presumably old PNe, it indicates that molecular hydrogen is likely to survive during a significant fraction of the life of an R-BPNe, only declining in the final stages of their nebular evolution.

The “longevity” of the  $H_2$  emission in R-BPNe is most likely linked with the true nature of molecular material in evolved bipolar PNe. The  $H_2$  emission does not come from a global PDR, but from a number of compact knots distributed into equatorial regions pervaded by ionized material. Molecular material survives in these knots and the  $H_2$  molecule is mostly excited by shocks. This is in agreement with the high-resolution images of the molecular material in NGC 2346 (Manchado et al. 2015). Similar structures are identified in the classical butterfly PN NGC 650-51, where the diffuse  $H_2$  emission is mostly tracing a ring which is composed of a set of knots and filamentary structures (Marquez-Lugo et al. 2015).

**Table 3.** H<sub>2</sub> fluxes for the IPHAS and Guerrero+2000 samples

Common name	PN G	Radius (pc)	d <sup>a</sup> (kpc)	F(Brγ) (× 10 <sup>15</sup> erg cm <sup>-2</sup> s <sup>-1</sup> )	F(H <sub>2</sub> ) (× 10 <sup>15</sup> erg cm <sup>-2</sup> s <sup>-1</sup> )	H <sub>2</sub> /Brγ	[N II]/Hα	BPN type	z (pc)	L(Brγ) (× 10 <sup>-30</sup> erg s <sup>-1</sup> )	L(H <sub>2</sub> ) (× 10 <sup>-30</sup> erg s <sup>-1</sup> )
PM 1-253	G035.4+03.4	0.29	6.9	<88	12.3	>0.14	...	W	407.32	499.57	70.06
...	G038.9-01.3	0.35	17.1	10.4	3.7	0.35	0.74	W	387.61	366.60	130.50
Te 6	G045.7+01.4	0.26	3.4	420	<6.1	<0.015	0.24	R	83.39	590.82	8.58
...	G045.7-03.8	1.82	6.4	5.1	43.2	8.5	4.35	R	426.54	25.26	215.85
Necklace	G054.2-03.4	0.72	6.9	20	1.9	0.093	0.47	R	409.57	113.46	10.67
Kn 7	G057.9-00.7	0.53	6.8	34	730	21.9	1.69	R	82.94	186.46	4088.80
...	G062.7+00.0	0.28	6.1	120	260	2.2	1.96	R	6.42	539.58	1172.70
...	G062.7-00.7	0.45	6.9	42	185	4.4	2.73	W	84.57	245.34	1071.03
...	G064.1-00.9	1.04	9.8	5.4	120	22.6	4.92	R	154.03	62.59	1419.02
...	G068.0+00.0	1.88	15.3	0.8	200	239.1	5.41	R	9.89	23.84	5704.47
...	G081.0-03.9	0.84	8.6	10	190	19.3	1.30	R	581.67	88.32	1701.08
...	G091.6-01.0	0.74	11.8	6.6	230	34.0	0.96	R	205.12	110.26	3758.30
...	G095.8+02.6	0.44	9.8	22	230	10.1	1.05	R	444.29	259.48	2634.17
...	G101.5-00.6	0.93	5.3	23	1.8	0.065	0.28	R	54.98	74.89	4.91
Príncipe de Asturias	G126.6+01.3	0.43	5.1	82	500	6.1	2.45	R	115.37	255.43	1556.61
M 1-57	G022.1-02.4	0.20	4.0	510	210	0.41	1.25	W	165.33	950.56	395.28
M 1-59	G023.9-02.3	0.16	2.9	1350	610	0.45	0.80	R	115.98	1,361.64	615.26
M 2-46	G024.8-02.7	0.24	4.2	330	110	0.33	1.00	W	196.58	687.67	231.33
PC 20	G031.7+01.7	0.14	3.8	900	530	0.58	0.80	R	113.21	1,582.68	932.02
M 4-14	G043.0-03.0	0.45	4.6	96	1920	20.0	1.77	R	242.89	249.97	4994.10
Hen 2-428	G049.4+02.4	0.38	2.6	370	<3.6	<0.010	0.47	R	110.38	312.99	3.05
K 3-34	G059.0+04.6	1.22	6.9	8.5	470	55.2	1.88	R	549.84	48.31	2667.92
M 1-91	G061.3+03.6	0.28	4.5	210	120	0.57	0.24	W	285.19	523.17	298.96
M 1-75	G068.0-00.0	0.39	2.6	380	3890	10.3	2.86	R	1.86	304.23	3139.09
K 3-58	G069.6-03.9	0.46	6.7	45	270	50.9	1.03	R	453.59	239.55	12192
NGC 6881	G074.5+02.1	0.17	3.3	880	>1250	>1.4	0.61	W	122.24	1,188.06	1679.95
M 4-17	G079.6+05.8	0.66	4.1	64	3240	50.6	0.65	R	415.75	130.81	6622.27
K 4-55	G084.2+01.1	0.65	4.5	54	2450	45.1	7.13	R	86.54	133.01	6012.67
M 2-52	G103.7+00.4	0.38	3.6	200	1980	9.7	1.79	R	25.06	317.51	3081.68
Bv 5-1	G119.3+00.3	0.46	4.6	92	1970	21.3	3.40	R	24.19	237.91	5077.89

<sup>a</sup> All distances computed according to Frew, Parker, & Bojičić (2016)**Figure 6.** Comparison of the H<sub>2</sub> and Brγ unabsorbed fluxes (*left*) and the H<sub>2</sub>/Brγ vs. [N II]/Hα line ratios (*right*) of the IPHAS PNe in this work and Guerrero et al. (2000)'s sample. Different symbols are used for the different data samples and morphologies as described in the left panel. Singular objects are labeled.

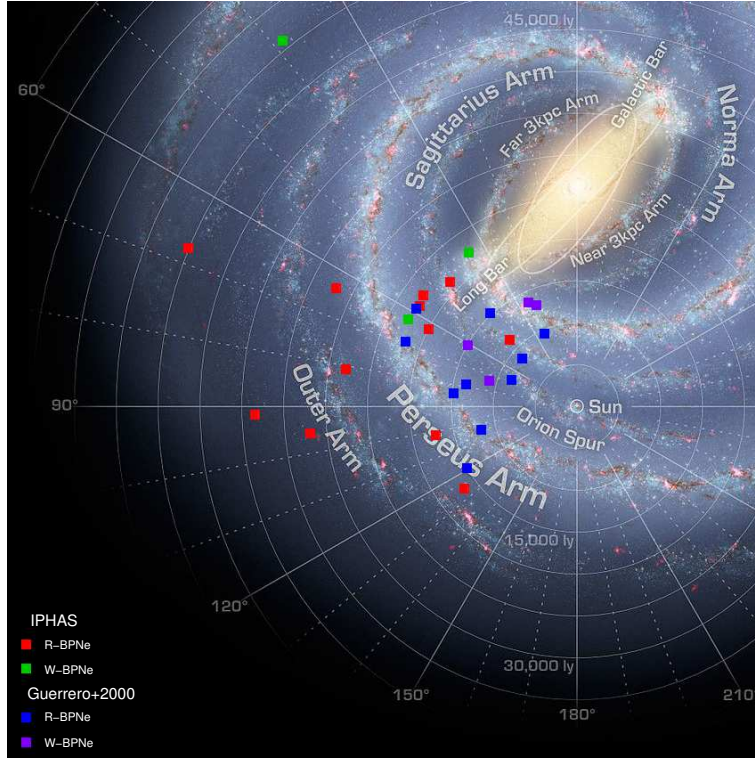


**Figure 7.** Distribution of the PNe in our sample in the Galaxy. The PNe have been located on an artistic view of the Milky Way (Image credit: NASA/JPL-Caltech/R. Hurt SSC/Caltech).

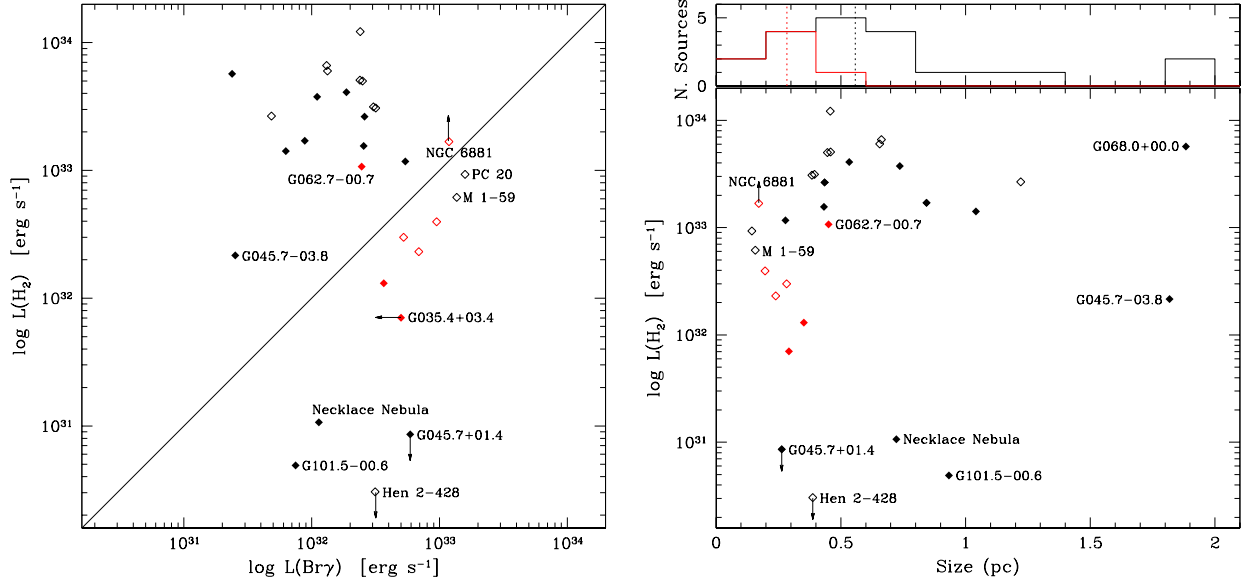


**Figure 8.** Comparison of the  $H_2$  and  $Br\gamma$  intrinsic luminosities (*left*) and distribution of nebular sizes with  $H_2$  luminosities (*right*). Different symbols are used for the different data samples and morphologies as described in the left panel of Figure 6. Singular objects are labeled.

#### 5.4 Bipolar PNe: two of a kind?

The results reported here confirm the dichotomy between bipolar PNe with broad rings and those with pinched waists first reported by Webster et al. (1988). Guerrero et al. (2000) questioned the origin of these two different branches of bipolar PNe, but it could not conclude whether W-BPNe and R-BPNe are different in nature or

are the same kind of sources, but found at different evolutionary stages.

The larger physical size of R-BPNe with respect to W-BPNe (Fig. 8-right) can be interpreted as evidence of the later evolutionary stage of R-BPNe with respect to W-BPNe.

To further confirm this observational fact, we have examined the PNe in the sample listed by Frew, Parker, & Bojčić (2016) and selected those with W-BPN and R-BPN morphologies. Their sizes

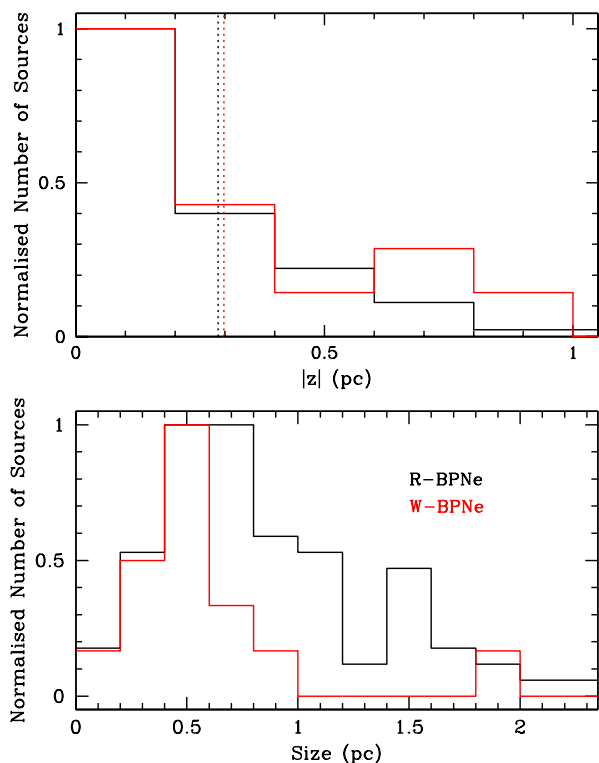


**Figure 9.** Distribution of the Galactic height (*top*) and size (*bottom*) of R-BPNe (black) and W-BPNe (red). The dotted vertical lines in the top panel correspond to the mean Galactic heights of the two samples of bipolar PNe.

have been derived using the angular sizes listed in this same reference and compared in Figure 9-*bottom*. This plot, based on a larger data sample, indeed confirms that R-BPNe are larger than W-BPNe.

There is limited information on the kinematics of the PNe in Table 3. Kinematic studies are only available for two W-BPNe (M 2-46 and NGC 6881, [Manchado, Stanghellini, & Guerrero 1996](#); [Guerrero & Manchado 1998](#)), but for nine R-BPNe (Hen 2-428, K 3-58, K 4-55, M 1-59, M 1-75, M 2-52, M 4-14, Necklace, and Príncipe de Asturias, [Weinberger 1989](#); [Guerrero, Manchado, & Serra-Ricart 1996](#); [Peña & Medina 2002](#); [Mampaso et al. 2006](#); [Dobrinčić et al. 2008](#); [Santander-García et al. 2010](#); [Corradi et al. 2011](#)). Using the new distances listed in Table 3, the innermost lobes of W-BPNe have kinematic ages between 1300 yrs (NGC 6881) and 6300 yrs (M 2-46), whereas for R-BPNe these range from 2100 yrs (Príncipe de Asturias) to 13800 yrs (K 4-55), with a mean kinematic age of 8000 yrs. These figures also suggest that R-BPNe are older than W-BPNe.

The larger  $H_2$  luminosity and  $H_2/Br\gamma$  ratio of R-BPNe with respect to W-BPNe can also be interpreted into an evolutionary scheme. The dominant  $H_2$  excitation mechanism in young PNe is UV fluorescence, because the density is not too high to collisionally de-excite the  $H_2$  molecules as in proto PNe (PPNe), but the nebular size is not too large to dilute the UV radiation field ([Natta & Hollenbach 1998](#)). Later on, as the PN keeps growing and the stellar luminosity declines, the local intensity of the UV radiation field is too low to produce significant UV excitation, whereas thermal emission from shock-excited hot  $H_2$  molecules prevails ([Natta & Hollenbach 1998](#)). The collisional excitation in the ionized regions of PNe with high CSPN temperatures ([Aleman & Gruenwald 2011](#)) can certainly enhance this excitation

among evolved PNe. These trends are observationally confirmed in samples of PNe at different evolutionary stages ([Davis et al. 2003](#)).

Can W-BPNe evolve into R-BPNe? [Balick \(1987\)](#) presented an evolutionary scheme for PNe, defining “*early*”, “*middle*”, and “*late*” PNe according to the relative distance of the bright inner rim to the central star. In this scheme, late bipolar PNe develop large bipolar lobes and achieve large aspect ratios. The average aspect ratios of R-BPNe ( $0.70 \pm 0.18$ ) and W-BPNe ( $0.60 \pm 0.27$ ) are, however, very similar. Actually, detailed hydrodynamic simulations of bipolar PNe do not support this interpretation of the evolution of bipolar PNe, as they achieve a shape early in their evolution that keeps growing with time ([Icke, Balick, & Frank 1992](#)) which is determined by the azimuthal density enhancement of the AGB wind ([Frank et al. 1993](#)). In this paradigm, W-BPNe do not evolve into R-BPNe, although it has been recognised that hydrodynamic models have great difficulties to reproduce the most axisymmetric bipolar PNe ([Balick 2000](#)). Other shaping agents (for instance, fast-moving knots and collimated outflows [Sahai & Trauger 1998](#); [Dennis et al. 2008](#)) have been proposed to be responsible of these extreme morphologies, but the time-evolution of the detailed morphology predicted in these scenarios has not been sufficiently explored.

Alternatively, W-BPNe and R-BPNe can evolve from different progenitor populations. This can be investigated by looking at the Galactic height distributions of R-BPNe and W-BPNe shown in Figure 9-*top*. R-BPNe and W-BPNe are mostly concentrated towards the Galactic Plane, with mean Galactic heights of  $290 \pm 310$  pc and  $300 \pm 270$  pc, respectively. As first described by [Corradi & Schwarz \(1995\)](#) and later on by [Kastner et al. \(1996\)](#), bipolar  $H_2$ -emitting PNe are concentrated towards the Galactic Plane. Although the Galactic height distribution of W-BPNe have a secondary peak at  $\sim 700$  pc, both samples have statistically consistent Galactic height distribution, indicating that they can be drawn from the same population of progenitor stars.

Even if W-BPNe and R-BPNe descend from the same progenitor population (relatively massive low- and intermediate-mass stars), they may have different progenitors. [Sahai et al. \(1991\)](#) proposed a two-fold formation mechanism for bipolar PNe, arguing that equatorial tori results from ‘born again’ disks formed through the destruction of planetary systems at the end of the AGB evolutionary phase.

The original amounts of dust in these sources can be very high, resulting in higher rates of  $H_2$  formation, although R-BPNe show a conspicuous absence of dust thermal emission.

Finally, it must be noted that a number of sources in our sample with low  $H_2/Br\gamma$  ratio, namely PNG 035.4+03.4, PNG 038.901.3, PNG 054.203.4, Hen 2-428, and M 1-91, have questionable PN nature. In this sense, it must be noted that the morphology of W-BPNe is strikingly similar to that of sources classified as SS, such as M 2-9 ([Schmeja & Kimeswenger 2001](#); [Rodríguez, Corradi, & Mampaso 2001](#); [Smith & Gehrz 2005](#); [Clyne et al. 2015](#); [Parker, Bojičić, & Frew 2016](#)), and that the scale height distribution of SS is similar to that of bipolar PNe ([Boiarchuk 1975](#); [Belczyński et al. 2000](#)). PNG 035.4+03.4 and M 1-91 have been classified as SS, whereas the PN nature of PNG 038.901.3 has been questioned ([Parker, Bojičić, & Frew 2016](#)). Otherwise, the central star of Hen 2-428 has been claimed to harbor a short-period double-degenerate core with combined mass above the Chandrasekhar limit ([Santander-García et al. 2015](#)), whereas PNG 054.203.4 (the Necklace Nebula) is suspected to have gone through a common envelope phase ([Miszalski et al. 2013](#)).

## 6 CONCLUSION

We have obtained deep near-IR observations of a sample of faint bipolar PNe selected from the IPHAS sample to search for H<sub>2</sub> emission. Molecular H<sub>2</sub> emission is found in most of them, mostly associated with the brightest nebular regions in equatorial rings, but also in bipolar lobes.

The present work also strengthens the dichotomy between H<sub>2</sub>-bright R-BPNe and H<sub>2</sub>-weak W-BPNe. A sample from the literature has been assembled to further investigate these two sub-classes of bipolar PNe. The excitation of W-BPNe is most likely caused by UV pumping, whereas R-BPNe are mostly excited by shocks. W-BPNe also show continuum emission at their central regions, but this is absent in R-BPNe. W-BPNe are not only intrinsically fainter in H<sub>2</sub> than R-BPNe, but they are also smaller and have lower kinematic ages. This suggests that W-BPNe are younger than R-BPNe, but it does not necessarily implies that W-BPNe evolve into R-BPNe. On the other hand, it seems they proceed from the same population of progenitor stars. The nature of many of those H<sub>2</sub>-weak bipolar PNe has been disputed, with a notable contamination of SS and post-common envelope binary systems.

The H<sub>2</sub> emission from bipolar PNe with broad equatorial rings is not associated with a classical PDR, but it rather comes from a discrete distribution of compact knots and filaments. The H<sub>2</sub> emission from these features is long-living, as the H<sub>2</sub> molecules in them survive long in the nebular evolution. As a result, their H<sub>2</sub> luminosity does not vary with the nebular expansion, i.e., with the nebular age.

## ACKNOWLEDGEMENTS

GR-L acknowledge support from Universidad de Guadalajara (Apoyo de Estancias Académicas – RG/003/2017), CONACyT, CGCI, PRODEP and SEP (Mexico). MAG acknowledges support of the grant AYA 2014-57280-P, co-funded with FEDER funds. He also acknowledges the hospitality of the Instituto de Astronomía y Meteorología of the Universidad de Guadalajara (Jalisco, Mexico). LS acknowledges support from PAPIIT grant IA-101316 (Mexico). ES acknowledge support from CONACyT and CUCEI (Mexico). This research has made use of the HASH PN database at hashpn.space. This paper makes use of data obtained as part of the INT Photometric H $\alpha$  Survey of the Northern Galactic Plane (IPHAS) carried out at the Isaac Newton Telescope (INT). The INT is operated on the island of La Palma by the Isaac Newton Group in the Spanish Observatorio del Roque de los Muchachos of the Instituto de Astrofísica de Canarias. All IPHAS data are processed by the Cambridge Astronomical Survey Unit, at the Institute of Astronomy in Cambridge. We thank Dr. Quentin Parker for detailed reading of the manuscript and useful comments.

## REFERENCES

Acosta Pulido J. A., et al., 2003, *INGN*, 7, 15  
 Akras S., Gonçalves D. R., Ramos-Larios G., 2017, *MNRAS*, 465, 1289  
 Aleman I., Gruenwald R., 2011, *A&A*, 528, A74  
 Balick B., 1987, *AJ*, 94, 671  
 Balick B., 2000, *ASPC*, 199, 41  
 Barentsen G., et al., 2014, *MNRAS*, 444, 3230  
 Beckwith S., Gatley I., Persson S. E., 1978, *ApJ*, 219, L33  
 Belczyński K., Mikołajewska J., Munari U., Ivison R. J., Friedjung M., 2000, *A&AS*, 146, 407  
 Black J. H., van Dishoeck E. F., 1987, *ApJ*, 322, 412

Bohlin R. C., Savage B. D., Drake J. F., 1978, *ApJ*, 224, 132  
 Boiarчук A. A., 1975, *IAUS*, 67, 377  
 Burton M. G., Hollenbach D. J., Tielens A. G. G., 1992, *ApJ*, 399, 563  
 Clyne N., Akras S., Steffen W., Redman M. P., Gonçalves D. R., Harvey E., 2015, *A&A*, 582, A60  
 Corradi R. L. M., Sabin L., Miszalski B., Rodríguez-Gil P., Santander-García M., Jones D., Drew J. E., Mampaso A., et al. 2011, *MNRAS*, 410, 1349  
 Corradi R. L. M., Schwarz H. E., 1995, *A&A*, 293, 871  
 Cox, P. et al. 1998, *ApJ*, 495, L23  
 Davis C. J., Smith M. D., Stern L., Kerr T. H., Chiar J. E., 2003, *MNRAS*, 344, 262  
 Dennis, T. J., Cunningham, A. J., Frank, A., et al. 2008, *ApJ*, 679, 1327-1337  
 Dickey J. M., Lockman F. J., 1990, *ARA&A*, 28, 215  
 Dinerstein H. L., Lester D. F., Carr J. S., Harvey P. M., 1988, *ApJ*, 327, L27  
 Dobrinčić M., Villaver E., Guerrero M. A., Manchado A., 2008, *AJ*, 135, 2199  
 Drew J. E., et al., 2005, *MNRAS*, 362, 753  
 Frank A., Balick B., Icke V., Mellema G., 1993, *ApJ*, 404, L25  
 Frew D. J., Parker Q. A., Bojičić I. S., 2016, *MNRAS*, 455, 1459  
 Froebrich D., et al., 2015, *MNRAS*, 454, 2586  
 Gledhill, T.M., et al. 2017, *IAU Symp.* 323, *Planetary Nebulae: Multi-Wavelength Probes of Stellar and Galactic Evolution*, *in press*.  
 González-Solares E. A., et al., 2008, *MNRAS*, 388, 89  
 Guerrero M. A., Manchado A., 1998, *ApJ*, 508, 262  
 Guerrero M. A., Manchado A., Serra-Ricart M., 1996, *ApJ*, 456, 651  
 Guerrero M. A., Villaver E., Manchado A., García-Lario P., Prada F., 2000, *ApJs*, 127, 125  
 Hora J. L., Latter W. B., 1994, *ApJ*, 437, 281  
 Hora J. L., Latter W. B., 1996, *ApJ*, 461, 288  
 Hora J. L., Latter W. B., Deutsch L. K., 1999, *ApJS*, 124, 195  
 Huggins P. J., Bachiller R., Cox P., Forveille T., 1996, *A&A*, 315, 284  
 Icke V., Balick B., Frank A., 1992, *A&A*, 253, 224  
 Kalberla P. M. W., Burton W. B., Hartmann D., Arnal E. M., Bajaja E., Morras R., Pöppel W. G. L., 2005, *A&A*, 440, 775  
 Karakas A. I., van Raai M. A., Lugaro M., Sterling N. C., Dinerstein H. L., 2009, *ApJ*, 690, 1130  
 Kastner J. H., Gatley I., Merrill K. M., Probst R., Weintraub D., 1994, *ApJ*, 421, 600  
 Kastner J. H., Weintraub D. A., Gatley I., Merrill K. M., Probst R. G., 1996, *ApJ*, 462, 777  
 Likkel L., Dinerstein H. L., Lester D. F., Kindt A., Bartig K., 2006, *AJ*, 131, 1515  
 Mampaso A., et al., 2006, *A&A*, 458, 203  
 Manchado A., et al., 2003, *RMxAC*, 16, 43  
 Manchado A., Stanghellini L., Guerrero M. A., 1996, *ApJ*, 466, L95  
 Manchado A., Stanghellini L., Villaver E., García-Segura G., Shaw R. A., García-Hernández D. A., 2015, *ApJ*, 808, 115  
 Marquez-Lugo R. A., Guerrero M. A., Ramos-Larios G., Miranda L. F., 2015, *MNRAS*, 453, 1888  
 Marquez-Lugo R. A., Ramos-Larios G., Guerrero M. A., Vázquez R., 2013, *MNRAS*, 429, 973  
 Matsuura M., Zijlstra A. A., Gray M. D., Molster F. J., Waters L. B. F. M., 2005, *MNRAS*, 363, 628  
 Matsuura M., et al., 2009, *ApJ*, 700, 1067  
 Miszalski B., Boffin H. M. J., Corradi R. L. M., 2013, *MNRAS*, 428, L39  
 Natta A., Hollenbach D., 1998, *A&A*, 337, 517  
 Osterbrock D. E., Ferland G. J., 2006, *Astrophysics of Gaseous Nebulae and Active Galactic Nuclei*, University Science Books, Sausalito, California  
 Parker Q. A., et al., 2006, *MNRAS*, 373, 79  
 Parker Q. A., Bojičić I. S., Frew D. J., 2016, *JPhCS*, 728, 032008  
 Peimbert M., Torres-Peimbert S., 1983, in Flower D. R., ed., *Planetary Nebulae Vol. 103 of IAU Symposium, Type I planetary nebulae*. pp 233–241  
 Peña M., Medina S., 2002, *RMxAA*, 38, 23  
 Peretto N., Fuller G., Zijlstra A., Patel N., 2007, *A&A*, 473, 207  
 Phillips J. P., Marquez-Lugo R. A., 2011, *MNRAS*, 410, 2257

- Phillips J. P., White G. J., Harten R., 1985, *A&A*, 145, 118  
Ramos-Larios G., Guerrero M. A., Miranda L. F., 2008, *AJ*, 135, 1441  
Ramos-Larios G., Guerrero M. A., Vázquez R., Phillips J. P., 2012, *MNRAS*, 420, 1977  
Rodríguez M., Corradi R. L. M., Mampaso A., 2001, *A&A*, 377, 1042  
Sabin L., 2008, PhD thesis, Jodrell Bank Centre for Astrophysics, University of Manchester, UK  
Sabin L., et al., 2014, *MNRAS*, 443, 3388  
Sahai R., Trauger J. T., 1998, *AJ*, 116, 1357  
Sahai R., Wootten A., Schwarz H. E., Clegg R. E. S., 1991, *A&A*, 251, 560  
Santander-García M., et al., 2010, *A&A*, 519, A54  
Santander-García M., Rodríguez-Gil P., Corradi R. L. M., Jones D., Miszalski B., Boffin H. M. J., Rubio-Díez M. M., Kotze M. M., 2015, *Natur*, 519, 63  
Schmeja S., Kimeswenger S., 2001, *A&A*, 377, L18  
Smith N., Balick B., Gehrz R. D., 2005, *ApJ*, 130, 853  
Smith N., Gehrz R. D., 2005, *AJ*, 129, 969  
Speck A. K., Meixner M., Fong D., McCullough P. R., Moser D. E., Ueta T., 2002, *AJ*, 123, 346  
Sternberg A., Dalgarno A., 1989, *ApJ*, 338, 197  
Viironen K., et al., 2009, *A&A*, 504, 291  
Webster B. L., Payne P. W., Storey J. W. V., Dopita M. A., 1988, *MNRAS*, 235, 533  
Weinberger R., 1989, *A&AS*, 78, 301  
Young K., Cox P., Huggins P. J., Forveille T., Bachiller R., 1999, *ApJ*, 522, 387  
Zuckerman B., Gatley I., 1988, *ApJ*, 324, 501